



HAL
open science

Unrivaled accuracy in measuring rotational transitions of greenhouse gases: THz CRDS of CF₄

Fabien Simon, A. Cuisset, Coralie Elmaleh, Francis Hindle, Gaël Mouret, Michael Rey, Cyril Richard, Vincent Boudon

► **To cite this version:**

Fabien Simon, A. Cuisset, Coralie Elmaleh, Francis Hindle, Gaël Mouret, et al.. Unrivaled accuracy in measuring rotational transitions of greenhouse gases: THz CRDS of CF₄. *Physical Chemistry Chemical Physics*, 2024, 10.1039/D4CP00653D . hal-04517326

HAL Id: hal-04517326

<https://u-bourgogne.hal.science/hal-04517326v1>

Submitted on 27 Mar 2024

HAL is a multi-disciplinary open access archive for the deposit and dissemination of scientific research documents, whether they are published or not. The documents may come from teaching and research institutions in France or abroad, or from public or private research centers.

L'archive ouverte pluridisciplinaire **HAL**, est destinée au dépôt et à la diffusion de documents scientifiques de niveau recherche, publiés ou non, émanant des établissements d'enseignement et de recherche français ou étrangers, des laboratoires publics ou privés.

Cite this: DOI: 00.0000/xxxxxxxxxx

Unrivalled accuracy in measuring rotational transitions of greenhouse gases: THz CRDS of CF₄[†]

Fabien Simon,^a Arnaud Cuisset,^{*a} Coralie Elmaleh,^a Francis Hindle,^a Gaël Mouret,^a Michaël Rey,^b Cyril Richard,^c and Vincent Boudon^c

Received Date
Accepted Date

DOI: 00.0000/xxxxxxxxxx

Tetrafluoromethane CF₄ is the most abundant perfluorocarbon in the atmosphere, where it is designated as PFC-14. This greenhouse gas is very stable, has an atmospheric lifetime of 50,000 years, and a high greenhouse warming potential 6500 times that of CO₂. Over the last 15 years, its atmospheric concentration has increased at a rate of 0.8 ppt/year. The accurate quantification of CF₄ is key to understanding the contribution of its emissions on the radiative forcing budget, the most precise spectroscopic parameters possible are hence required. In this study, a novel high finesse THz cavity, providing an interaction length in excess of 1 km, has enabled highly resolved spectra, and quantification of the weak transitions of CF₄ by Cavity Ring-Down Spectroscopy (CRDS). More than 50 pure rotational $P_6 - P_6 : \nu_3 - \nu_3$ lines of CF₄ have been measured, yielding both position and intensity with unequalled precision. Several tetrahedral splitting are fully resolved and measured with sub-MHz accuracy. Moreover, CRDS-THz allows determining absolute intensities and, using a global fit of the ν_2 polyad series, a CF₄ dipole parameter, namely $\bar{\mu}_{3,3}$, has been fitted to 106.38(53) mD. This value is in a very good agreement with that of the *ab initio*-based parameter deduced from a dipole moment surface. For the first time, a set of *ab initio* effective dipole moment parameters is derived for the computation of the transitions of the type $P_n - P_n$ ($n = 0, \dots, 8$) and the resulting line list composed of 25 863 transitions can be used to model the whole CF₄ rotational spectrum. Finally, the TFMCaSDa database is updated and is available for future spectroscopic and monitoring activities.

1 Introduction

It is generally accepted in the public consciousness that greenhouse gas is synonymous with carbon dioxide CO₂. The media warn of the need to reduce CO₂ emissions. All over the world, Carbon Capture Use and Storage (CCUS) technologies are being developed to achieve zero-carbon emissions, CO₂ being the principal target. However, the global warming contribution of other greenhouse gases, which may be less abundant than CO₂, is far from negligible. This is typically the case for tetrafluoromethane CF₄: with an atmospheric concentration almost five million times weaker than CO₂, this molecule has a warming power 6500 times greater and a lifetime 200 times longer (50,000 years) in the

atmosphere¹. Although less abundant, CF₄'s residual radiative forcing is much greater, and our atmosphere takes much longer to get rid of it. As a result, we can expect CF₄'s contribution to global warming from greenhouse gases to increase over the next few years. A study published in 2016 warned of a slowdown in the decline in perfluorocarbons (PFC) emissions, and urged PFC generating industries especially aluminium and semiconductor manufacturing to continue to reduce the emissions of these potent greenhouse gases, which, once emitted, will stay in the atmosphere essentially permanently (on human timescales) and contribute to radiative forcing². More recently, long-lived atmospheric greenhouse gases have been compared using IASI/Metop and ACE-FTS satellite and AGAGE ground-based measurements over the last 15 years³. These three instruments were found to demonstrate a remarkable degree of agreement monitoring the atmospheric CF₄, the concentration is increasing linearly at a rate of 0.8 ppt/year ($\approx 1\%$ of the average atmospheric concentration) since 2008. These analyses were based on the inversion of the absorption spectrum of the strong ν_3 stretching fundamental band of CF₄ observed in the 1283 cm⁻¹ region¹.

Therefore, the accuracy of the CF₄ monitoring depends on

^a Laboratoire de Physico-Chimie de l'Atmosphère, UR 4493, LPCA, Université du Littoral Côte d'Opale, F-59140 Dunkerque; E-mail: arnaud.cuisset@univ-littoral.fr

^b Groupe de Spectrométrie Moléculaire et Atmosphérique, UMR CNRS 7331, BP 1039, F-51687, Reims Cedex 2, France

^c Laboratoire Interdisciplinaire Carnot de Bourgogne, UMR 6303 CNRS - Université de Bourgogne, 9 Av. A. Savary, BP 47870, F-21078 Dijon Cedex, France

[†] Electronic Supplementary Information (ESI) available: (1) Full list of fitted effective Hamiltonian parameters. (2) Room-temperature CF₄ line list in the range 4–82 cm⁻¹ calculated from an *ab initio* effective model. See DOI: 10.1039/cXCP00000x/

the accuracy of modelling of the ν_3 rovibrational band including line frequencies, intensities, air-broadening coefficients and profiles up to high J levels. In addition to the fundamental band, the main hot bands involving the lower rovibrational levels such as $\nu_3 + \nu_i - \nu_i$ with $i = 1, 2$ and 4 must be included since they contribute 92 % of the total absorption at room temperature. This was the objective of a study in which a global analysis of 17 rovibrational bands of CF_4 was undertaken⁴. The first Terahertz (THz) measurements of the very weak rotational transitions of CF_4 in the $\nu_3 = 1$ state ($\nu_3 - \nu_3$ hot band) were included. Synchrotron-based Fourier Transform spectroscopy was used with an optical path of 150 m with a White-type multipass cell, allowing to record $R(20)$ to $R(37)$ line clusters in the 20–37 cm^{-1} (600–921 GHz) region at a resolution of 0.1 cm^{-1} . Due to a lack of sensitivity and resolution, the recorded THz lines were pressure-broadened ($P \approx 100$ mbar) and largely averaged (5000 co-additions)⁵. As a result, these measurements are characterised by high levels of uncertainty both in frequency and in intensity. Moreover, the tetrahedral splitting of CF_4 rotational lines was only very partially resolved. More recently, it has been demonstrated⁶ that THz Fabry-Perot absorption spectroscopy with a km effective pathlength allowed to detect CF_4 THz lines with intensities lower than $1 \times 10^{-27} \text{cm}^{-1} / (\text{molecule} \cdot \text{cm}^{-2})$ and to fully resolve the tetrahedral splitting. In this study, only the $R(20)$ cluster was measured with the unique consideration of line frequencies.

Here, a similar experimental setup described previously⁷ is used, a Cavity Ring-Down Spectroscopy (CRDS) configuration has enabled the direct measurement of the absorption coefficient⁸. $R(19)$ to $R(30)$ and $Q(32)$ to $Q(34)$ line clusters are measured both in frequency and intensity with unequalled precision. CRDS THz line frequencies and intensities are included in a global fit of the ν_2 polyad (see subsection 5.1) allowing an improvement of the RMS deviation and an accurate determination of the $\mu_{3,3}$ dipole moment parameter specific to the $\nu_3 - \nu_3$ CF_4 transitions. Fluoride-containing molecules are heavy species with highly congested spectra composed of many hot bands, even at room temperature. Recently, the complete elucidation of the dense and complex band structure in the rotationally-resolved spectra of the greenhouse CF_4 and SF_6 molecules was made possible using accurate *ab initio* and variational calculations^{9,10}. In this work, a non-empirical, *ab initio*-based effective model has been derived for the first time for the modelling of the whole CF_4 rotational spectrum. The quality of the resulting calculated line list has been validated by a direct comparison with experiment. Finally, this work has enabled an updated line list of CF_4 to be tabulated in the TFMecaSDa database while the *ab initio* predictions pave the way for future experimental studies and line-by-line analyses.

2 THz Cavity Ring-Down spectrometer

Observation of the weak CF_4 transitions around 20 cm^{-1} is beyond the sensitivity limits of a standard spectrometer with a single path absorption cell¹¹. To undertake high-resolution measurements of weakly absorbing species in this region, we have developed a cavity assisted THz spectrometer^{7,8}. The excellent resolution is provided by an electronic source, which is an amplified multiplier chain (AMC). A standard microwave synthesizer

is used to feed the AMC with 0 dBm in the range from 7.92 to 8.75 GHz. Once the frequency of the synthesizer has been multiplied by the AMC ($\times 72$) it directly addresses the range from 570 to 630 GHz, or 19 to 21 cm^{-1} . Typical power levels in the rectangular waveguide at the AMC output are -2 dBm. The excellent resolution that can be achieved by such sources is possible due to its spectral purity, the emission linewidth is estimated to be around 1 kHz. Up-converting a microwave synthesizer provides two useful advantages. Firstly, it allows the source to be readily modulated in both frequency and amplitude, and secondly a traceable reference frequency can be easily introduced, in our case a timing signal generated by a GPS receiver (Spectracom EC20S) was employed.

In order to increase the available sensitivity and consequently the accuracy of line measurements, a high finesse cavity was used to extend the interaction length between the sample gas and the THz radiation. The cavity is composed of two photonic mirrors and a corrugated waveguide, both designed for operation around 20 cm^{-1} . The radiation from the AMC source is launched into free space with a horn antenna before being coupled to the cavity using a TPX lens, see Figure 1. The output of the cavity is refocused by a second TPX lens onto a Zero Biased Detector (ZBD). The cavity has a free spectral range of 310 MHz, finesse values of 4000 are routinely obtained, providing an interaction length of 1.2 km for a measurement cell that has a physical length of around 50 cm. To measure the narrow molecular transitions, both the AMC frequency and cavity mode must be simultaneously scanned over the zone of interest. This is achieved by finely adjusting the cavity length by means of two piezoelectric actuators, further details can be found elsewhere⁷. This instrument can not only be used to make Cavity Enhanced Absorption Spectroscopy (CEAS) measurements but also CRDS, the latter is of particular interest and has been used for this study as it directly gives a quantitative value of the absorption coefficient⁸.

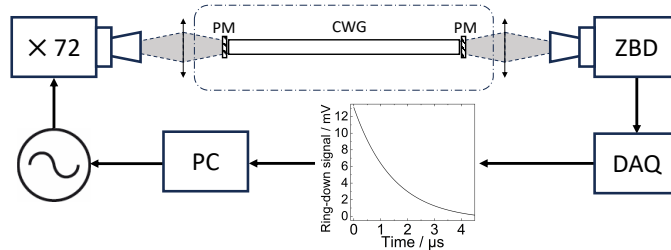


Fig. 1 THz Cavity Ring-Down Spectroscopy setup. An AMC source coupled to a resonant cavity, itself composed of two Photonic Mirrors (PM) and a Corrugated Waveguide (CWG). The output of the cavity is measured by a ZBD whose signal is recorded by a Data Acquisition system (DAQ). The cavity is placed inside a low pressure gas chamber, as indicated by the dash-dot line.

The principle of CRDS is to measure the residency time τ of the photons in the cavity. The presence of an absorbing gas in the cavity will lead to a decrease in τ compared to the initial value under vacuum conditions. To measure the cavity ring-down time τ the AMC must be coupled to the cavity to allow the intracavity power to build up. Once a stable power level is obtained the source must be rapidly removed, achieved using a pulse modu-

lation, and the acquisition process is triggered. The light exiting the cavity is measured as a function of time and averaged for a large number of ring-down events, in our case 5×10^4 events per second. The signal from the detector is amplified, then measured by a dedicated data acquisition card (Spectrum Instruments) that samples at 1.25 GS/s and calculates the average waveform in real time. Each average waveform is fitted by an exponential function to give the value of τ .

3 Experimental results

Pure CF_4 (>99.997%) purchased from Messer was introduced into the empty measurement chamber. A pressure of 0.2 mbar was selected to maximise the molecular signal while maintaining narrow line widths, optimising the available molecular Signal to Noise Ratio (SNR). The cavity is sensitive to temperature which results in slow changes to the baseline. A second spectrum is recorded, with an empty chamber, immediately after the acquisition of the molecular spectrum. The total duration is a compromise between the degree of data accumulation that is employed and the minimisation of the variation of the baseline. The measurement of a single line with its baseline is typically completed within 10 minutes. If no baseline spectrum is available a synthetic baseline can be produced using a suitable low order polynomial function. All CRDS spectra have been obtained at room temperature (294.0(15) K), with a frequency step size of 100 kHz. This step size was selected to match the mode width of the cavity, which provides around 20 measurement points within the FWHM of the lines. A typical example spectrum with its baseline is shown in Figure 2. The difference in the cavity Ring-Down time with and without the gas is clearly distinguished for three molecular lines of CF_4 separated by about 7 MHz (0.0002 cm^{-1}). The equivalent interaction length here is calculated to be 850 m with a cavity finesse of 2800. A total of 54 transitions, from 577.405 GHz to 629.164 GHz (19.26 cm^{-1} to 20.99 cm^{-1}), have been probed in this study. Nineteen of them are isolated so have been individually resolved, while the remaining 35 could not be individually isolated due to the Doppler broadening at room temperature ($\approx 0.8 \text{ MHz}$ (FWHM)). In this case, the measured absorption results from two or three overlapping molecular transitions. The use of CRDS has enabled the quantification of 28 (single or multiplet) line intensities.

The cavity Ring-Down time with and without gas, $\tau(\nu)$ and $\tau_0(\nu)$ respectively, are directly related to the molecular absorption coefficient $\alpha(\nu)$ (cm^{-1})¹²:

$$\alpha(\nu) = \frac{1}{c} \left(\frac{1}{\tau(\nu)} - \frac{1}{\tau_0(\nu)} \right) \quad (1)$$

where c is the speed of light (cm/s) and, ν the frequency (Hz) of the radiation. CRDS does not require a calibrated sample in order to perform quantitative absorption measurements. Knowledge of the physical length of the cavity is also not necessary. For the previous example $\alpha(\nu)$ is calculated directly from the CRDS spectrum and baseline and is shown in Figure 3. Alternatively, the spectrum in Figure 4 corresponds to 3 transitions of CF_4 with less than 100 kHz between the calculated line centres. The Doppler broadening of $\text{FWHM}_{\text{Doppler}} = 823 \text{ kHz}$ prevents the individual transi-

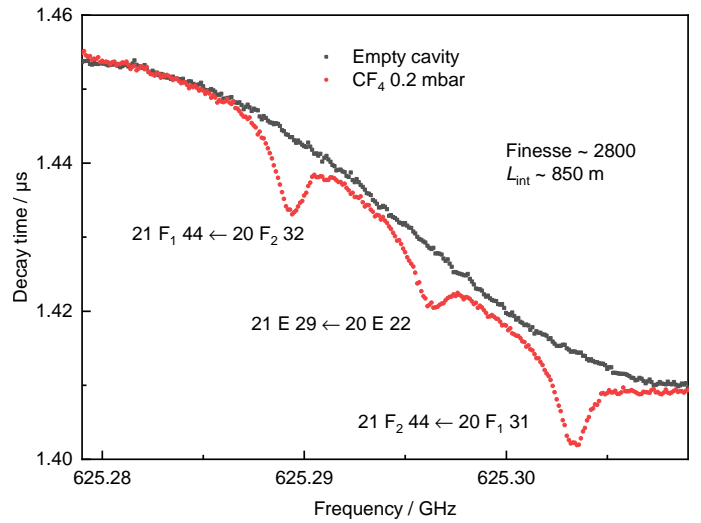


Fig. 2 A CRDS spectrum and its baseline probing 3 rotational transitions of CF_4 . Black points, cavity under vacuum conditions. Red points, CF_4 at 0.2 mbar. Each point is the average of 10^5 ring-down events. Step size 100 kHz, total acquisition time 600 s.

tions from being resolved. This line displays a peak absorption of around $2.6 \times 10^{-7} \text{ cm}^{-1}$ resulting from a change of 30 ns in τ . Here the mirrors are operating in the centre of the forbidden band optimising the cavity performance with $\tau = 2 \mu\text{s}$, a finesse of 3900, and an interaction path length of 1.2 km from a 48 cm length cavity. The smallest quantifiable variation in α is estimated to be $2 \times 10^{-8} \text{ cm}^{-1}$ for this configuration.

The spectra measured in this way are fitted with a Voigt profile, whose parameters are all free other than Doppler broadening which is fixed to its calculated value. No Voigt profile variations may be observed due to the limited SNR of the weak intensities of the CF_4 rotational transitions. The integrated absorption coefficient $A = \int \alpha \, d\nu$ in cm^{-2} , line centre frequency ν_{exp} and line width in cm^{-1} are extracted from the fitting procedure. The transition line intensity I_{exp} is determined by dividing A to the molecular density n in $\text{molecule} \cdot \text{cm}^{-3}$ determined by the gas equation $n = \frac{P}{k_B T}$, while ν_{exp} is compared with the calculated value ν_{calc} , as presented in Table 1. The precision of ν_{exp} is estimated using the measured line width and SNR, as explained in the following section. For multiplet lines, we indicate in Table 1 the different assignments and calculated frequencies; we detail this case in Section 5.2 below. For example, in Figure 4, the three transitions are fitted using a single Voigt function of fixed Gaussian contribution.

4 Uncertainties

The experimental uncertainty of ν_{exp} is evaluated by Eq. 2 where FWHM is line width, and $\delta\nu$ the frequency step size¹³.

$$\Delta\nu_{\text{exp}} = \frac{0.979\sqrt{\text{FWHM}}\delta\nu}{\text{SNR}} \quad (2)$$

The FWHM is obtained from the Voigt fitting procedure, and in our case $\delta\nu$ was held constant at 100 kHz. As regards to the evaluation of the SNR, a prudent estimation was adopted. The

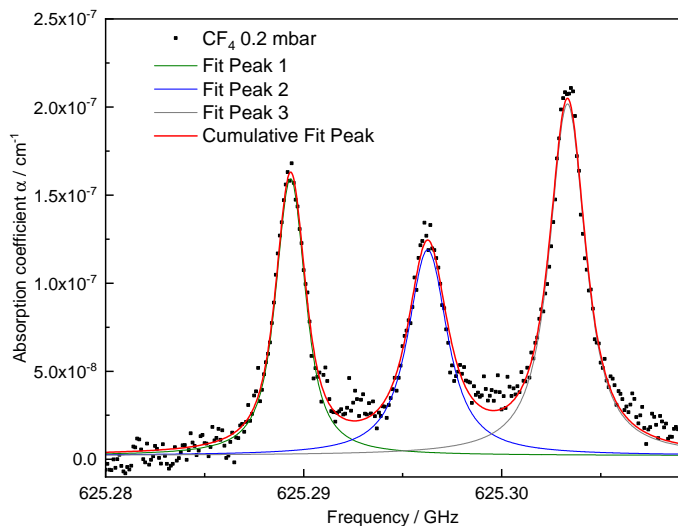


Fig. 3 The absorption coefficient spectrum and baseline determined from the CRDS spectrum in Figure 2. Three Voigt functions sharing the same Gaussian line broadening contribution are used to obtain the cumulative fit of these transitions with overlapping tails, (21 F_1 44 \leftarrow 20 F_2 32), (21 E 29 \leftarrow 20 E 22), and (21 F_2 44 \leftarrow 20 F_1 31).

signal amplitude was simply the maximum value of the absorption coefficient. The Noise amplitude was determined from the maximum peak-to-peak value present in first and last 5 percent of the spectrum.

The line intensity uncertainty ΔI_{exp} was calculated by taking into account the precision of the pressure gauge, knowledge of the measurement cell temperature and the quality of the fitted absorption profile. The pressure gauge error is smaller than 0.001 mbar, and the temperature was controlled at 294.0(15) K. The quality of the fit is limited by the stability of the baseline which is not always perfectly removed, as can be observed in Figure 4. The Voigt profile was minimised using OriginLab[®] software which provides a confidence interval ΔA equal to the estimated standard deviation of A . The different contributions were combined by Eq. 3 and are included in Table 1.

$$\frac{\Delta I_{\text{exp}}}{I_{\text{exp}}} = \frac{\Delta A}{A} + \frac{\Delta T}{T} + \frac{\Delta P}{P} \quad (3)$$

The average relative uncertainties of the CRDS measurements are $\approx 10^{-5}$ % for the frequencies and ≈ 10 % for the intensities. Compared to the synchrotron FT-FIR measurements¹⁴, the frequency and intensity uncertainties are improved by factors 200 and 2, respectively. In a weighted global fit including IR data, such an accuracy improvement yields to a significant influence of the THz rotational lines even with a modest number of lines. This was demonstrated for the THz measurements of the CH_4 centrifugal distortion induced rotational transitions¹⁵, in the case of CF_4 it will be verified in section 5.1.

5 Analysis and discussion

The idea of introducing effective Hamiltonians $\tilde{H}(\vec{r})$ for the modelling of absorption spectra of molecules whose energy levels are organized as small groups of nearly degenerate vibrational states,

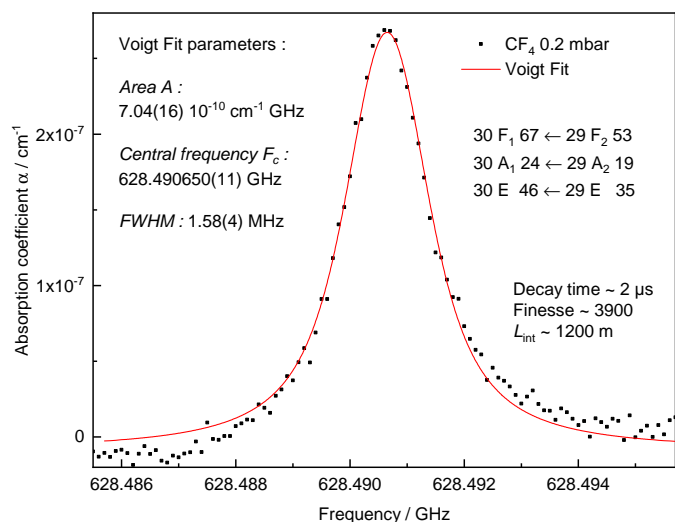


Fig. 4 Absorption spectrum of 3 CF_4 transitions, the line centred frequencies are separated by less than 100 kHz so they cannot be resolved due to the Doppler broadening. Acquisition with a step size of 100 kHz, and 1×10^5 ring-down events are averaged to obtain a single frequency point, a total acquisition time of 220 s is required to obtain complete spectrum. A single Voigt function with a fixed Gaussian contribution is used to fit the absorption profile.

called polyads, is well established for decades^{16,17}. Currently, there exists two different ways for constructing effective Hamiltonians:

- Case 1:* Effective parameters of a phenomenological model are obtained by a direct fit to experiment using a least-squares method (see Section 5.1). The same holds for the construction of an effective dipole moment operator (see Section 5.2). In this context, the approach proposed in Ref. 18 is relevant for spherical top molecules.
- Case 2:* A non-empirical effective model is derived by applying a series of unitary transformations to the nuclear-motion Hamiltonian, composed of a kinetic energy operator and an *ab initio* potential energy surfaces (PES). Here, the numerical method proposed in Ref. 19 is preferred to the commonly-used Van Vleck transformations because the dipole moment parameters can be obtained from a dipole moment surface (DMS) without performing tedious algebraic calculations (see Section 5.3).

For both cases, each polyad is characterized by a polyad number

$$P = c_1 v_1 + c_2 v_2 + \dots + c_{N_m} v_{N_m} \quad (c_i \in \mathbb{R}_{>0}), \quad (4)$$

and the associated set of Hamiltonian parameters $\{\vec{r}\}_P$ is obtained either by direct fitting to experimental data (*Case 1*) or from *ab initio* PESs (*Case 2*). In Eq. (4), v_i are the vibrational quantum numbers and N_m the number of vibrational modes. By definition, the first polyad is $P = 0$, or simply denoted as P_0 . Although the second polyad does not necessarily equal $P = 1$, it is denoted as P_1 , and so on. The success in the line-by-line analysis of high-resolution spectra thus lies in a convenient choice of the polyad vector $\mathbf{c} = (c_1, c_2, \dots, c_{N_m})^t$ in order to include the most relevant resonance coupling terms. In the case of quite isolated polyads

Table 1 Experimentally observed line frequencies ν_{exp} and intensities I_{exp} compared with the calculated values (ν_{calc} , I_{calc}) obtained from the fit (see Sections 5.1 and 5.2). $I_{\text{ab initio}}$ are the intensities obtained from the *ab initio* effective model (see Section 5.3). For unresolved line clusters, the experimental intensity I_{exp} is that of the cluster as a whole and the intensity of each component can be obtained through Eq. (7). Line frequencies are given in GHz. Line intensities in units of $\text{cm}^{-1} / (\text{molecule} \cdot \text{cm}^{-2})$ which have been multiplied by 1×10^{27} . The experimental uncertainties are given in parenthesis.

| J'' | Transition | | | ν_{exp} GHz | ν_{calc} GHz | $I_{\text{exp}} \times 10^{27}$ $\text{cm}^{-1} / (\text{molecule} \cdot \text{cm}^{-2})$ | $I_{\text{calc}} \times 10^{27}$ $\text{cm}^{-1} / (\text{molecule} \cdot \text{cm}^{-2})$ | $I_{\text{ab initio}} \times 10^{27}$ $\text{cm}^{-1} / (\text{molecule} \cdot \text{cm}^{-2})$ | | |
|-----|----------------|------------|----|---------------------------|----------------------------|--|---|--|------|-----------|
| | C'' | α'' | J' | | | | | | C' | α' |
| 19 | A ₂ | 11 | 20 | A ₁ | 15 | 595.825800(106) | 595.825626 | 4.57(54) | 3.75 | 4.22 |
| 19 | A ₂ | 12 | 20 | A ₁ | 16 | 596.518640(272) | 596.518587 | 3.00(54) | 2.71 | 3.05 |
| 19 | A ₁ | 10 | 20 | A ₂ | 14 | 595.848490(110) | 595.848163 | 2.77(56) | 3.69 | 4.14 |
| 19 | F ₂ | 30 | 20 | F ₁ | 41 | 595.832630(175) | 595.832384 | 2.77(55) | 2.24 | 2.51 |
| 19 | F ₂ | 31 | 20 | F ₁ | 42 | 596.205100(285) | 596.205017 | 1.32(30) | 1.91 | 2.15 |
| 19 | F ₁ | 31 | 20 | F ₂ | 42 | 595.840010(179) | 595.839828 | 2.85(48) | 2.23 | 2.50 |
| 19 | F ₁ | 32 | 20 | F ₂ | 43 | 596.114480(329) | 596.114288 | - | - | - |
| 19 | F ₁ | 33 | 20 | F ₂ | 44 | 596.311630(380) | 596.311646 | - | - | - |
| 20 | A ₂ | 11 | 21 | A ₁ | 14 | 625.730970(39) | 625.731006 | 4.62(25) | 3.50 | 3.93 |
| 20 | A ₁ | 12 | 21 | A ₂ | 16 | 625.584540(48) | 625.584555 | 4.96(36) | 3.77 | 4.29 |
| 20 | A ₁ | 13 | 21 | A ₂ | 17 | 626.471100(47) | 626.471092 | 2.04(21) | 2.21 | 2.49 |
| 20 | E | 22 | 21 | E | 29 | 625.296260(75) | 625.296234 | 1.74(23) | 1.65 | 1.86 |
| 20 | E | 24 | 21 | E | 31 | 626.464170(165) | 626.464052 | - | - | - |
| 20 | F ₂ | 32 | 21 | F ₁ | 44 | 625.289340(57) | 625.289361 | 2.54(25) | 2.48 | 2.80 |
| 20 | F ₂ | 33 | 21 | F ₁ | 45 | 625.656590(91) | 625.656716 | 2.01(22) | 2.09 | 2.45 |
| 20 | F ₂ | 34 | 21 | F ₁ | 46 | 625.839690(78) | 625.839690 | 2.10(28) | 1.97 | 2.29 |
| 20 | F ₁ | 31 | 21 | F ₂ | 44 | 625.303320(50) | 625.303327 | 3.38(23) | 2.47 | 2.77 |
| 20 | F ₁ | 32 | 21 | F ₂ | 45 | 625.617060(80) | 625.617183 | 1.93(19) | 2.20 | 2.50 |
| 20 | F ₁ | 34 | 21 | F ₂ | 47 | 626.466270(116) | 626.466375 | - | - | - |
| 27 | A ₁ | 16 | 28 | A ₂ | 21 | | 587.307807 | | 1.94 | 2.23 |
| 27 | E | 33 | 28 | E | 43 | 587.307750(110) | 587.307609 | 4.21(43) | 0.77 | 0.89 |
| 27 | F ₁ | 51 | 28 | F ₂ | 64 | | 587.307807 | | 1.16 | 1.32 |
| 27 | F ₂ | 48 | 28 | F ₁ | 63 | 589.437590(73) | 589.437532 | 4.19(27) | 1.58 | 1.82 |
| 27 | F ₁ | 50 | 28 | F ₂ | 65 | | 589.437528 | | 1.58 | 1.83 |
| 28 | A ₂ | 17 | 29 | A ₁ | 21 | | 610.106098 | | 2.77 | 3.20 |
| 28 | E | 34 | 29 | E | 44 | 610.106060(38) | 610.106093 | 5.64(26) | 1.11 | 1.27 |
| 28 | F ₂ | 51 | 29 | F ₁ | 67 | | 610.106095 | | 1.66 | 1.91 |
| 28 | A ₁ | 16 | 29 | A ₂ | 19 | | 586.724152 | | 1.64 | 1.77 |
| 28 | E | 30 | 29 | E | 35 | 586.724190(71) | 586.724132 | 3.21(28) | 0.66 | 0.70 |
| 28 | F ₁ | 44 | 29 | F ₂ | 53 | | 586.724139 | | 0.99 | 1.05 |
| 29 | A ₂ | 16 | 30 | A ₁ | 19 | | 606.278291 | | 2.35 | 2.53 |
| 29 | E | 30 | 30 | E | 37 | 606.278270(41) | 606.278287 | 4.27(20) | 0.94 | 1.00 |
| 29 | F ₂ | 45 | 30 | F ₁ | 53 | | 606.278288 | | 1.41 | 1.51 |
| 29 | A ₂ | 19 | 30 | A ₁ | 24 | | 628.490594 | | 2.18 | 2.52 |
| 29 | E | 35 | 30 | E | 46 | 628.490650(36) | 628.490688 | 4.72(29) | 0.87 | 1.00 |
| 29 | F ₂ | 53 | 30 | F ₁ | 67 | | 628.490657 | | 1.31 | 1.50 |
| 30 | A ₂ | 16 | 31 | A ₁ | 19 | | 626.603820 | | 1.84 | 1.98 |
| 30 | E | 32 | 31 | E | 37 | 626.603890(49) | 626.603964 | 3.52(22) | 0.74 | 0.79 |
| 30 | F ₂ | 48 | 31 | F ₁ | 58 | | 626.603916 | | 1.11 | 1.19 |
| 30 | F ₂ | 47 | 31 | F ₁ | 57 | 626.381980(35) | 626.381977 | 3.63(24) | 1.48 | 1.58 |
| 30 | F ₁ | 46 | 31 | F ₂ | 55 | | 626.381973 | | 1.48 | 1.58 |
| 31 | A ₁ | 16 | 31 | A ₂ | 24 | | 577.405098 | | 2.21 | 2.46 |
| 31 | E | 32 | 31 | E | 47 | 577.405100(148) | 577.405104 | 3.74(54) | 0.88 | 0.99 |
| 31 | F ₁ | 49 | 31 | F ₂ | 70 | | 577.405102 | | 1.33 | 1.48 |
| 32 | A ₁ | 18 | 32 | A ₂ | 24 | | 592.046796 | | 1.70 | 1.90 |
| 32 | E | 34 | 32 | E | 49 | 592.046540(64) | 592.046330 | 3.11(20) | 0.68 | 0.76 |
| 32 | F ₁ | 50 | 32 | F ₂ | 73 | | 592.046486 | | 1.02 | 1.14 |
| 32 | F ₂ | 50 | 32 | F ₁ | 72 | 594.991100(118) | 594.991007 | 3.73(52) | 1.36 | 1.52 |
| 32 | F ₁ | 49 | 32 | F ₂ | 74 | | 594.991008 | | 1.36 | 1.52 |
| 33 | A ₂ | 18 | 33 | A ₁ | 24 | | 612.305429 | | 2.31 | 2.55 |
| 33 | E | 34 | 33 | E | 50 | 612.305440(49) | 612.305457 | 4.69(22) | 0.93 | 1.03 |
| 33 | F ₂ | 51 | 33 | F ₁ | 76 | | 612.305448 | | 1.39 | 1.54 |
| 34 | F ₂ | 53 | 34 | F ₁ | 77 | 629.163980(66) | 629.163941 | 2.76(20) | 1.39 | 1.55 |
| 34 | F ₁ | 52 | 34 | F ₂ | 78 | | 629.164005 | | 1.39 | 1.55 |

with few vibrational bands, the approach proposed in (Case 1) allows to obtain very accurate results using few parameters. Conversely, for more complex polyads containing many vibrational bands, a proper characterization of all the resonance couplings

becomes a challenging task. In that case, missing information on the so-called “dark” states may lead to a poor determination of some resonance coupling parameters, making the approach defined in (Case 2) more relevant.

Note that the accuracy of the *ab initio* effective parameters $\{\tilde{\tau}\}_P^{ab\text{ initio}}$ derived in (Case 2) is typically that of the PES. These parameters can be thus further optimized by fine tuning to experimental data as in (Case 1). We can also mention that for heavy molecules like CF_4 the density of lines dramatically increases because of the tremendous number of hot bands, resulting in strongly congested spectra, even at room temperature.

5.1 Inclusion in the global fit of line positions

Here, we used the present high-precision line positions to include them in the so-called “ ν_2 ” polyad scheme already used in Ref. 4. This scheme corresponds to a polyad vector $\mathbf{c} = (0, 2, 6, 3)^t$ in which the $\nu_3 = 1$ level falls into the P_6 polyad (along with $\nu_4 = 2$). We can notice that in this scheme, the ν_1 mode is ignored and there is no P_1 polyad (see discussion in Section 5.4).

The general theory of the tensorial effective Hamiltonian can be found in many papers. The reader can for instance refer to Ref. 18 and references therein. Let us just recall that for each polyad P_k , the effective Hamiltonian can be written in the form

$$\tilde{H}_{\{P_k\}} = \sum_{\text{all indexes}} t_{\{s\}\{s'\}}^{\Omega(K, n\Gamma)\Gamma_v\Gamma'_v} \beta \left[\varepsilon V_{\{s\}\{s'\}}^{\Omega_v(\Gamma_v\Gamma'_v)\Gamma} \otimes R^{\Omega(K, n\Gamma)} \right] (A_1). \quad (5)$$

In this equation, the $t_{\{s\}\{s'\}}^{\Omega(K, n\Gamma)\Gamma_v\Gamma'_v}$ are parameters to be determined, while $\varepsilon V_{\{s\}\{s'\}}^{\Omega_v(\Gamma_v\Gamma'_v)\Gamma}$ and $R^{\Omega(K, n\Gamma)}$ are vibrational and rotational operators, respectively. For each term, Ω_v and Ω represent the degree in elementary vibrational operators (creation a^+ and annihilation a operators), and rotational operators (components J_x , J_y and J_z of the angular momentum), respectively. β is a factor that allows the scalar terms (terms with $\Gamma = A_1$, the totally symmetric irreducible representation of T_d) to match the “usual” contributions like $B_0 J^2$, etc. The order of each individual term is defined as $\Omega + \Omega_v - 2$.

Using this theory, we simply added the 54 $\nu_3 - \nu_3$ (as part of $P_6 - P_6$ transitions) line positions of Table 1 in the same “ ν_2 ” global fit as in Ref. 4 (see in particular Table 5 of this reference), using the XTDS²⁰ software package. We also took this opportunity to “clean” the fit by removing many duplicate assignments. A few $\nu_3 - \nu_3$ line positions that were already present in the fit were replaced with values from the present work. Thus, the $P_6 - P_6$ assignments has raised from 268 to 316. In Table 2, we compare the new fit statistics with those of Ref. 4. Figure 5 displays the fit residuals for line positions for the different transitions included in this global fit. Figure 6 details the $\nu_3 - \nu_3$ ($P_6 - P_6$) part.

Although the combination of both the elimination of duplicate lines and the introduction of the present new high-precision THz lines renders the comparison with the previous work somewhat tricky, we can tell that (i) we start from a more reliable line assignment list and (ii) the $\nu_3 - \nu_3$ region fit is influenced by the new lines. The overall root mean squares (RMS) deviation in THz region has slightly decreased from 33.64 to 31.43 MHz. The 4.976 weighted standard deviation for the new THz lines may seem high, but this is due to strong constraints between data with very diverse experimental precisions in this fit; anyway, their RMS deviation of ca. 99 kHz is satisfactory. Some RMS deviations for other transitions have slightly increased compared to

Ref. 4, but, again, this is due to the “cleaning” of the global fit that has changed the weight of many lines with the removal of duplicates. In any case, it was mandatory to re-do the global fit of line positions in order to obtain consistent eigenvectors for the line intensity analysis. We give the full list of effective Hamiltonian parameters resulting from the present fit as supplementary material.

5.2 Fit of effective dipole moment parameter

As a spherical top, CF_4 has no permanent dipole moment. But, following the same theory as the one explained in Ref. 5, we consider here the effective dipole moment operator for $\nu_3 - \nu_3$ transitions in the form

$$\begin{aligned} \tilde{\mu}^{\langle \mu_3 - \mu_3 \rangle} &= \tilde{\mu}_{\{\text{GS}-\text{GS}\}}^{\langle \mu_3 - \mu_3 \rangle} + \tilde{\mu}_{\{\nu_3 - \nu_3\}}^{\langle \mu_3 - \mu_3 \rangle} \\ &= \tilde{\mu}_0 R^{2(2, F_2)} + \tilde{\mu}_{3,3} V_{\{3\}\{3\}}^{2(F_2 F_2) F_2} + \dots \end{aligned} \quad (6)$$

This contains two terms in the right member. The first one, $\mu_{\{\text{GS}-\text{GS}\}}^{\langle \mu_3 - \mu_3 \rangle}$ corresponds to a centrifugal distortion-induced dipole moment in the Ground State (GS) and should be very small. The second term is the dipole moment derivative that is specific to $\nu_3 - \nu_3$ transitions. The corresponding parameter $\mu_{3,3}$ can be fitted using the present intensity data.

The main problem when fitting effective dipole moment parameters using experimental data is that one needs to find and assign isolated lines in order to determine intensities of single transitions. However, as previously mentioned, for quite heavy molecules, there are generally line clusters consisting of superimposed transitions that cannot be resolved experimentally. This is the case for CF_4 . Let us take an example from Table 1: the line at $587.307750 \text{ cm}^{-1}$ is a triplet consisting of an $A_1 \rightarrow A_2$, an $E \rightarrow E$ and an $F_1 \rightarrow F_2$ transition. But the measured intensity, $4.21 \times 10^{27} \text{ cm}^{-1} / (\text{molecule.cm}^{-2})$ is the sum for these three transitions. Among the 30 measures intensities, 13 are such multiplets: 4 doublets and 9 triplets, the remaining 17 measurements corresponding to singlets. We have thus a potential of 52 transitions (which is much better than just using the 17 isolated lines), if we can extract individual line intensities for the multiplets. This is possible, since we know their assignments, that is the transitions that compose them. The idea is to split experimental intensities between the multiplet components using the following procedure.

Due to the 1/2 spin of the F ligands, the CF_4 have spin statistical weights w_i for each T_d symmetry species A_1 , A_2 , E , F_1 or F_2 . It is easy to show²³ that these weights are 3, 3, 2, 5 and 5, respectively. Thus, for a cluster of $n = 2$ or 3 lines with experimental total intensity I_{exp} , the intensity of the “subline” i can be extracted as:

$$I_{\text{exp}}^i = \frac{w_i I_{\text{exp}}}{\sum_{j=1}^n w_j}. \quad (7)$$

We thus obtained 52 individual line intensities that we introduced in a fit, again using XTDS²⁰. The 2 transitions $20 F_2 43 \leftarrow 19 F_1 32$ (the line is too distorted to be fitted) and $20 F_2 44 \leftarrow 19 F_1 33$ ($I_{\text{exp}} = 1.15 \times 10^{-27} \text{ cm}^{-1} / (\text{molecule.cm}^{-2})$, uncertainty 34%) shown in Table 1 have not been taken in consideration for the line strength global fit, for experimental reasons (very low

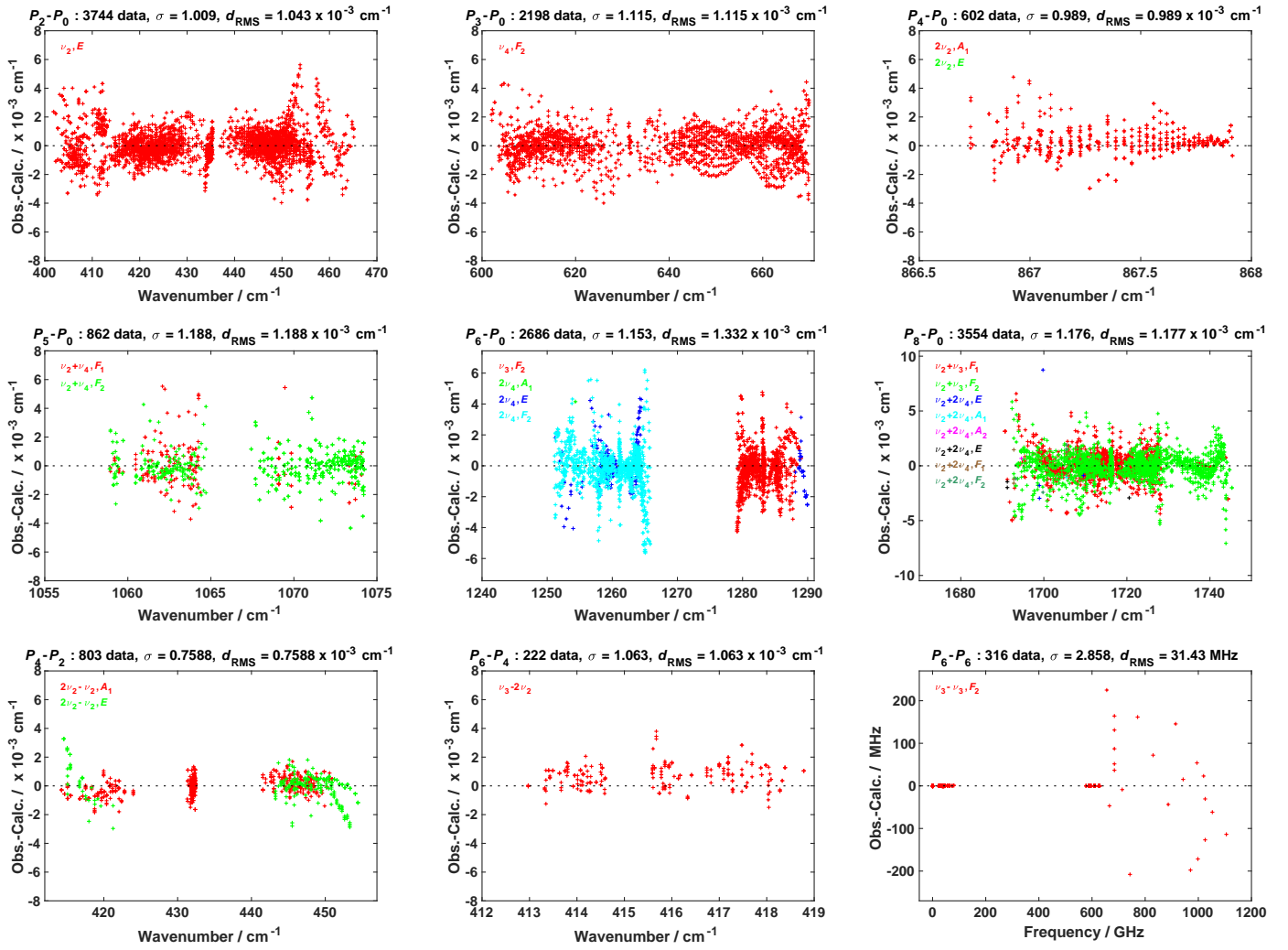


Fig. 5 Fit residuals for line positions in the global fit; each panel corresponds to a set of transitions between two polyads (see text for polyad definition); σ is the dimensionless standard deviation and d_{RMS} the root mean square deviation. This is to be compared with the equivalent Figure 3 in Ref. 4.

Table 2 Fit statistics for line positions in the “ ν_2 ” polyad scheme, compared to results of Ref. 4. σ is the dimensionless standard deviation and d_{RMS} the root mean square deviation in $1 \times 10^{-3} \text{ cm}^{-1}$, except for THz $\nu_3 - \nu_3$ lines for which it is given in MHz.

| Transitions | Ref. 4 | | | | This work | | | |
|--|----------|------------------|----------|---|-----------|------------------|----------|---|
| | Nb. data | J_{max} | σ | $d_{\text{RMS}} / 1 \times 10^{-3} \text{ cm}^{-1}$ | Nb. data | J_{max} | σ | $d_{\text{RMS}} / 1 \times 10^{-3} \text{ cm}^{-1}$ |
| $P_2 - P_0 : \nu_2$ | 4686 | 82 | 0.9984 | 1.027 | 3744 | 82 | 1.009 | 1.043 |
| $P_3 - P_0 : \nu_4$ | 2254 | 72 | 1.276 | 1.276 | 2198 | 72 | 1.115 | 1.115 |
| $P_4 - P_0 : 2\nu_2$ | 823 | 42 | 0.7757 | 0.7757 | 602 | 42 | 0.989 | 0.989 |
| $P_5 - P_0 : \nu_2 + \nu_4$ | 877 | 39 | 1.188 | 1.188 | 862 | 39 | 1.188 | 1.188 |
| $P_6 - P_0 : \nu_3 / 2\nu_4$ | 2930 | 53 | 0.9847 | 1.161 | 2686 | 53 | 1.153 | 1.332 |
| $P_8 - P_0 : \nu_2 + (\nu_3 / 2\nu_4)$ | 4763 | 49 | 1.167 | 1.167 | 3554 | 49 | 1.176 | 1.177 |
| $P_4 - P_2 : 2\nu_2 - \nu_2$ | 803 | 68 | 0.7758 | 0.7758 | 803 | 68 | 0.7588 | 0.7588 |
| $P_6 - P_4 : \nu_3 - 2\nu_2$ | 222 | 37 | 1.189 | 1.189 | 222 | 37 | 1.063 | 1.063 |
| $P_6 - P_6 : \nu_3 - \nu_3$ | 268 | 37 | 0.9173 | 33.64 MHz | 316 | 37 | 2.858 | 31.43 MHz |
| Total | 17626 | 82 | 1.076 | 1.116 | 14987 | 82 | 1.159 | 1.126 |

finesse attributed to a misalignment of the mirrors; one mirror may have hit against the waveguide during the experiment). It also appeared that two lines intensities were outliers that were removed from that fit. These 2 transitions, $21 E 31 \leftarrow 20 E 24$ and $21 F_2 47 \leftarrow 20 F_1 34$, separated by only 2.1 MHz, they are

too close from each other to be reliably fitted for quantification*.

* NB: A multi Voigt fit with fixed frequency centers gives respectively $I_{\text{exp}} = 8.71 \times 10^{-28} \text{ cm}^{-1} / (\text{molecule.cm}^{-2})$ uncertainty 17 % and $I_{\text{exp}} = 1.11 \times 10^{-27} \text{ cm}^{-1} / (\text{molecule.cm}^{-2})$ uncertainty 15 %. If the frequency centres are let free, the fit gives

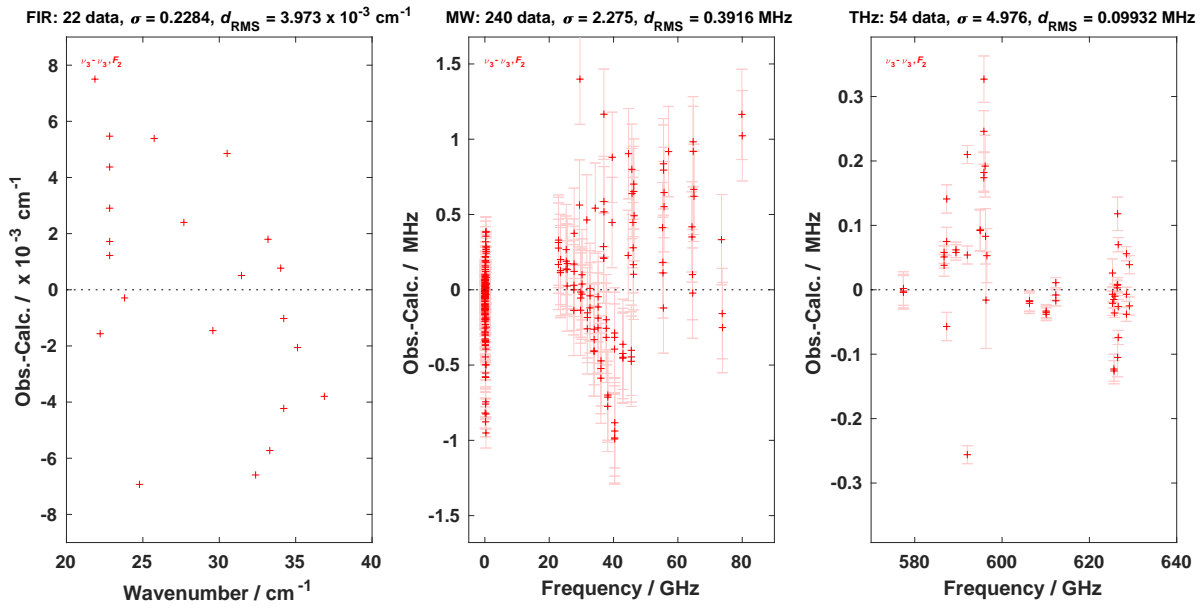


Fig. 6 Fit residuals for line positions in the global fit in the case of $P_6 - P_6$; σ is the dimensionless standard deviation and d_{RMS} the root mean square deviation. The three panels detail these residuals for far-infrared (FIR) lines from Ref. 5, infrared-microwave/radiofrequency (MW) lines from Refs. 21,22 and THz line from the present work. The last two panels also display experimental line position error bars. It should be noticed that Ref. 4 did not mention the MW lines from Takami *et al.* but those were already included in the global fit of this paper.

Those four transitions have been included in the global fit of line positions but, consequently, we finally end up with a fit of 50 experimental intensities. The resulting relative root mean square deviation is 16.6 % and the standard deviation is 1.706. We obtain the following parameter:

$$\tilde{\mu}_{3,3} = 106.38(53) \text{ mD}. \quad (8)$$

This value is somewhat higher than the 80 mD from Ref. 5, but this one was a very rough estimate that did not result from a fit. All attempts to fit higher-order effective dipole moment terms were unsuccessful. The *ab initio* calculations presented in Section 5.3 confirmed that the next term in $(R^{1(1,F_1)} \otimes V_{3,3}^{F_2 F_2(F_1)})(F_2)$ gives a contribution 4 orders of magnitude smaller than the pure vibrational term (8). To our knowledge this is the very first time that a dipole moment parameter on CF_4 is fitted using directly intensity measurements for individual lines. Figure 7 displays the fit residuals for line intensities. We see no systematic deviation as a function of the rotational quantum number J , confirming that there is not further fittable term using the present data. Figure 8 compares the experimental intensities with the calculated ones, using either the above parameter or the *ab initio* lines (see Section 5.3 below). We also checked that the calculated far-infrared spectrum using the fitted effective dipole moment parameters compares well to the experimental spectrum from Ref. 5, as shown on Figure 9, to be compared with Figure 1 of this previous paper. We used here a better simulation program²⁴ that better takes into account the instrumental parameters from the Fourier-transform spectrometer. This explains that the previous

simulation, obtained thanks to a rougher simulation underestimated the parameter value. The spectrum calculated from the *ab initio* effective model described in Section 5.3 is also depicted in Figure 9.

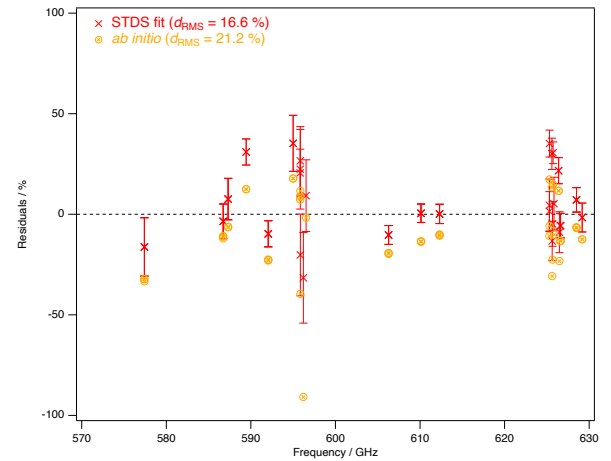


Fig. 7 Relative fit residuals for fitted and *ab initio* line intensities for the presently measured $\nu_3 - \nu_3$ THz lines, as a function of the frequency.

5.3 Derivation of *ab initio* effective dipole moment parameters

In Ref. 9, more than 700 vibrational bands and subbands were predicted for CF_4 to construct a variationally-computed line list up 4000 cm^{-1} , composed by 2 billion rovibrational transitions at 296 K. Such a density of lines is obtained in methane spectra at 1000 K²⁶. This list is freely available on the TheoReTS²⁷ webpages <https://theorets.univ-reims.fr>, [uncertainties of the order of 1 million %.](https://theorets.</p>
</div>
<div data-bbox=)

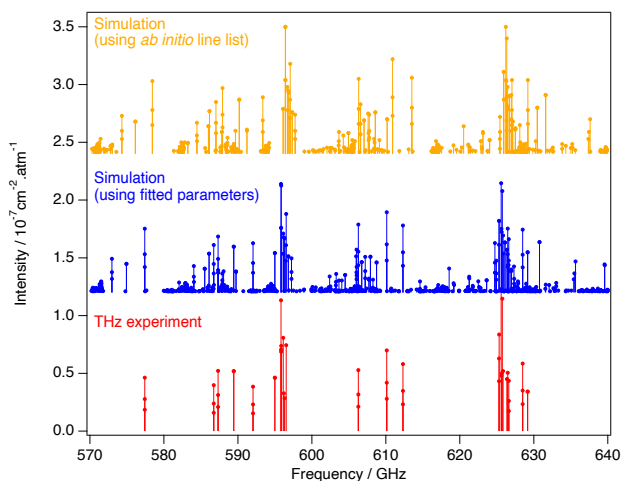


Fig. 8 Comparison between THz experimental, fitted (using effective Hamiltonian and dipole moment) and *ab initio* lines computed in Section 5.3. Simulated lines have been shifted upward for clarity.

tsu.ru. The accuracy of our *ab initio* line intensities was recently validated in different spectral ranges by a direct comparison with experiment²⁸. Due to its relatively low-lying vibrational modes compared to other spherical top molecules like methane, the CF₄ rotational spectrum is composed by successive hot band transitions of the type $P_n - P_n$ ($n = 1, 2, \dots$). We have fitted the parameter μ_{33} (8) of $P_6 - P_6$ using the “ ν_2 ” polyad scheme.

For the modelling of the very crowded CF₄ spectra, we can consider an approach which is complementary to the one presented in Sections 5.1 and 5.2 and that combines both the small dimensionality of the spectroscopic models and the completeness of the variational calculation. Within that context, a novel methodology has been recently proposed in Ref. 19 to construct an *ab initio* effective rotation-vibration spectroscopic model directly from a PES and a DMS. Very briefly, let $\mathbf{H}^{(J,C)}$ the matrix representation of the complete nuclear-motion Hamiltonian for a given symmetry block (J, C) , computed in a basis set $\{|\gamma; J, C\rangle\}$ where γ denotes all other symmetry labels and quantum numbers (ν_i , etc.). For the CF₄ molecule, the *ab initio* PES and DMS of Ref. 9 were employed and the Eckart-Watson Hamiltonian²⁹ was used to build $\mathbf{H}^{(J,C)}$ using harmonic oscillator basis functions. Then, we search for a unitary transformation $\mathcal{T}_P^{(J,C)}$ that brings $\mathbf{H}^{(J,C)}$ into block diagonal form up to a maximum polyad P_{N_P} .

$$\begin{aligned} \mathbf{H}_{\text{Polyad}}^{(J,C,P)} &= [\mathcal{T}_{P'}^{(J',C')}]^{-1} \mathbf{H}^{(J,C)} \mathcal{T}_P^{(J,C)} \\ &= [\mathbf{H}_{P_0}^{(J,C)} \oplus \dots \oplus \mathbf{H}_{P_{N_P}}^{(J,C)}] \oplus \mathbf{H}_R^{(J,C)}, \end{aligned} \quad (9)$$

by defining a consistent polyad scheme. In Eq. (9), the last block \mathbf{H}_R includes all the “remaining” polyads beyond P_{N_P} . Unlike contact transformations³⁰ based on perturbation theory³¹, the approach proposed in Ref. 19 obviates the need to make tedious algebraic calculations for the derivation of both Hamiltonian and dipole moment effective parameters. A brief inspection of the harmonic frequencies for CF₄ suggests to define the polyad vector as $\mathbf{c} = (0.8, 0.4, 1.2, 0.6)^t$. Using this scheme, the first polyads are: P_0 =ground state, $P_1 = \nu_2$, $P_2 = \nu_4$, $P_3 = \{\nu_1, 2\nu_2\}$, $P_4 = \nu_2 + \nu_4$,

$P_5 = \{\nu_1 + \nu_2, 3\nu_2, \nu_3, 2\nu_4\}$, etc. In this paper, the matrix $\mathbf{H}_{\text{Polyad}}^{(J,C,P)}$ was constructed up to $P_{N_P} = P_8$ from a numerical procedure that took 5 hours using 28 processors, including the variational calculation up to $J = 10$ to compute $\mathcal{T}_P^{(J,C)}$. The choice of this polyad scheme compared to the one proposed in Section 5.1 will be discussed in Section 5.4.

At this stage, it is worth mentioning that $\mathbf{H}_{\text{Polyad}}^{(J,C,P)}$ in Eq. (9) is nothing but a matrix representation of an effective Hamiltonian in a basis $\{|\gamma; J, C, P\rangle\}$, with a set of parameters $\{\tilde{t}\}_P^{ab \text{ initio}}$ to be determined. The strategy thus consists in considering an effective Hamiltonian $\tilde{H}(\tilde{t})$ of the type (5) whose the effective parameters are determined for each polyad P such that the matrix elements of $\tilde{H}(\tilde{t})$ match the elements of $\mathbf{H}_{\text{Polyad}}^{(J,C,P)}$. To this end, we follow the iterative procedure (19) of Ref. 19. For line intensity calculation, we can define the transformed matrix

$$\tilde{\mathbf{M}}_{\Theta} = [\mathcal{T}_{P'}^{(J',C')}]^{-1} \mathbf{M}_{\Theta} \mathcal{T}_P^{(J,C)}, \quad (10)$$

where \mathbf{M}_{Θ} ($\Theta = X, Y, Z$) is the matrix of the laboratory-fixed frame dipole moment components $(C^{(\Gamma')} \otimes M^{(\Gamma)})^{(\tilde{\Gamma})}$ computed in the same primitive basis as the Hamiltonian. Here, $M_{\alpha}^{(\Gamma)} \equiv M_{\alpha}^{(\Gamma)}(\mu)$ ($\alpha = x, y, z$) are the molecular-fixed frame dipole moment components and the μ 's are the *ab initio* DMS parameters of Ref. 9. $C^{(\Gamma')}$ is the tensor counterpart³² of the direction cosines $\lambda_{\Theta\alpha}$. Similarly, we determine the parameters $\tilde{\mu}$ of an effective normal-mode dipole moment operator $\tilde{M}_{\alpha}^{(\Gamma)}(\tilde{\mu})$ (see Eq. (6)) such that the matrix elements of $(C^{(\Gamma')} \otimes \tilde{M}^{(\Gamma)})^{(\tilde{\Gamma})}$ match $\tilde{\mathbf{M}}_{\Theta}$. Only transitions with $J \leq 2$ are required to determine the effective dipole moment parameters.

In this work, we have developed the effective Hamiltonian (5) at order 8 up to the eighth polyad, except that the resulting 964 parameters have been determined directly from the PES, without any fit. The effective dipole moment of the type (6) has been expanded at order 6 and 723 vibrational parameters were simultaneously determined from the DMS for all the transitions $P_n - P_n$, $n = 0, \dots, 8$. We have shown in this work that the contribution of the rovibrational terms to the line intensities of $P_n - P_n$ was negligible, by at least 4 orders of magnitude. Only one rotational parameter was included in the model for computing the $P_0 - P_0$ transitions and one rovibrational parameter was determined for $\nu_2 - \nu_2$, for which purely vibrational terms are not allowed by symmetry. Some terms of the tensor dipole moment are given below,

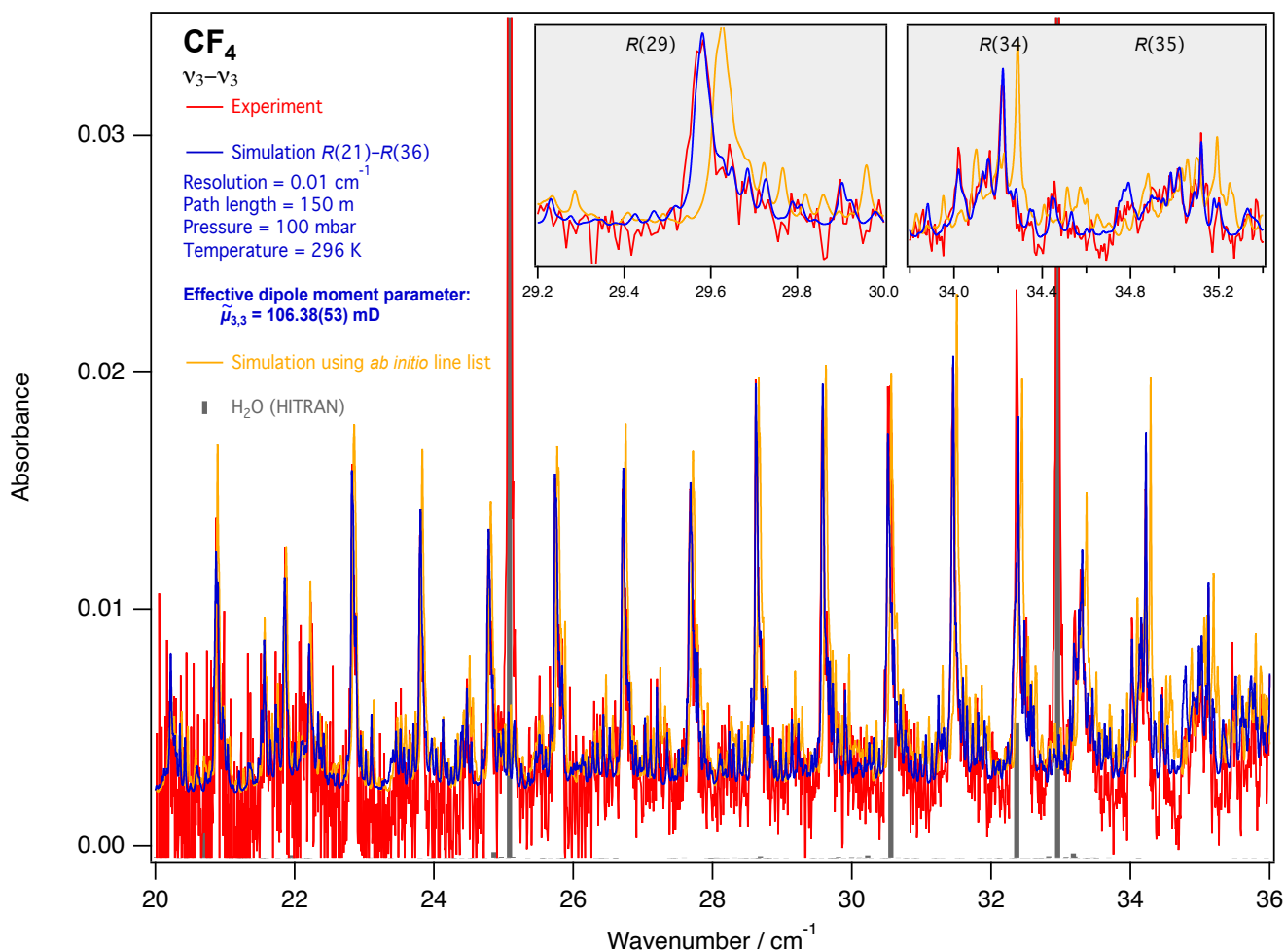


Fig. 9 FTIR spectrum of $\nu_3 - \nu_3$ lines in the R branch (from Ref. 5), compared to the simulation. Grey ticks show water lines taken from the HITRAN database²⁵. The inserts detail three line clusters. The *ab initio* line list – with errors on the line positions estimated between 0.01 and 0.05 cm^{-1} – can be found in Supplementary Material.

with parameters in units of 10^{-4} Debye:

$$\begin{aligned}
 \nu_3 - \nu_3(P_5 - P_5) &\rightarrow 680.07 V_{\{3,3\}}^{F_2 F_2(F_2)} + \dots \\
 \nu_3 - 2\nu_4(P_5 - P_5) &\rightarrow 5.80 V_{\{3,44\}}^{F_2 A_1(F_2)} \\
 &\quad - 3.23 V_{\{3,44\}}^{F_2 E(F_2)} + \dots \\
 2\nu_4 - 2\nu_4(P_5 - P_5) &\rightarrow 7.22 V_{\{44,44\}}^{F_2 F_2(F_2)} \\
 &\quad + 8.45 V_{\{44,44\}}^{F_2 A_1(F_2)} + \dots \\
 3\nu_2 - \nu_3(P_5 - P_5) &\rightarrow 0.49 V_{\{222,3\}}^{A_1 F_2(F_2)} \quad (11) \\
 &\quad - 0.17 V_{\{222,3\}}^{E F_2(F_2)} + \dots \\
 4\nu_2 - \nu_2 + \nu_3(P_7 - P_7) &\rightarrow -0.24 V_{\{2222,23\}}^{A_1 F_2(F_2)} \\
 &\quad + 0.36 V_{\{2222,23\}}^{E F_2(F_2)} + \dots \\
 \nu_2 + \nu_3 - \nu_2 + \nu_3(P_7 - P_7) &\rightarrow 961.11 V_{\{23,23\}}^{F_2 F_2(F_2)} + \dots \\
 \nu_3 + \nu_4 - \nu_3 + \nu_4(P_8 - P_8) &\rightarrow 10.72 V_{\{34,34\}}^{F_2 F_2(F_2)} + \dots
 \end{aligned}$$

Note that the definition of the irreducible tensor vibrational op-

erators³³ used in Eq. (11) differs from that in Eq. (6) whereas the rotational part in the effective Hamiltonian and dipole moment operator is unchanged. We can show that these two sets of vibrational operators can be related by following Appendix of Ref. 19. We have plotted in Fig. 10 (upper panel) the strongest line intensities between 5 and 80 cm^{-1} using the *ab initio* dipole moment parameters. The line positions were computed from the pure *ab initio* effective Hamiltonian parameters at an accuracy estimated between 0.01 and 0.05 cm^{-1} . The line list is provided in Supplementary Material. Finally, in the experimental spectral range considered in this work, only $\nu_3 - \nu_3$ transitions have been observed (see Fig. 10, bottom panel). The corresponding *ab initio* effective parameter can be easily converted to the STDS formalism as

$$\tilde{\mu}_{3,3}^{ab \text{ initio}} = 117.8 \text{ mD}. \quad (12)$$

The error between this value and that obtained from the fit in Eq. (8) is close to 10%, which is within the RMS error of 16.6%. Fig. 8 shows the good agreement between the observed lines and those computed from the fitted and *ab initio* models, though the *ab initio* line positions were not computed at the spectroscopic

accuracy. With the actual limit of detection of the THz CRDS technique, line intensities below $1 \times 10^{-27} \text{ cm}^{-1} / (\text{molecule.cm}^{-2})$ are difficult to measure (see Table 1). Fig. 10 explains why only $\nu_3 - \nu_3$ transitions were observed in the $19 \text{ cm}^{-1} - 21 \text{ cm}^{-1}$ region. This also explains why — contrary to CH_4 ^{34,35} — the GS–GS and $\nu_4 - \nu_4$ transitions cannot be observed here because their associated parameters turn out to be 3 and 2 orders of magnitude smaller than those of methane, respectively. For example, our *ab initio* parameter μ_0 involved in (6) is estimated to $\sim 0.056 \mu\text{D}$ while the recommended value for methane is of $\sim 22.5 \mu\text{D}$.

Line intensities of $\nu_3 - \nu_3$ in the observed spectral range and computed from the parameter $\tilde{\mu}_{3,3}^{ab \textit{ initio}}$ are given in the last column of Tab. 1. We can also compute the experimental and calculated (fit and *ab initio*) sum of intensities $S (\times 10^{26})$ in this range. We obtain $S_{\text{exp}} = 9.36$, $S_{\text{fit}} = 8.87$ and $S_{ab \textit{ initio}} = 9.91 \text{ cm}^{-1} / (\text{molecule.cm}^{-2})$ and we can see that S_{exp} is between the two calculated values. Note that the two calculated sums differ by 10.5% while a comparison between the fitted parameter $\tilde{\mu}_{3,3}$ (8) and the *ab initio* parameter $\tilde{\mu}_{3,3}^{ab \textit{ initio}}$ (12) would suggest a difference of 21%. A brief inspection of the eigenvector decomposition showed that the treatment of the resonance coupling for the dyad system $\nu_3/2\nu_4$ slightly differs between the fitted and *ab initio* effective models. This thus explains why the difference between $S_{ab \textit{ initio}}$ is not that expected.

5.4 Effective versus “*ab initio*” polyad scheme: discussion

The choice of a relevant polyad scheme (4) is partly conditioned by the available observed data. In Ref. 4 and in this work, the so-called “ ν_2 ” polyad scheme was employed to build the empirically-fitted effective Hamiltonian and dipole moment because of the lack of data for ν_1 . The same hold for the bands $\nu_1 + \nu_2$ and $3\nu_2$ which were omitted in the polyad called P_5 . For the construction of the *ab initio* model presented in Section 5.3, only PES and DMS are required. By definition, all the resonance couplings are taken into account in the *ab initio* model, even those associated with “dark” states that are not directly observable. Thus, the choice (4) based on some “resonance” conditions between the vibrational modes does not depend on available experimental data.

The “*ab initio*” polyad vector $(0.8, 0.4, 1.2, 0.6)^t$, also equals to $(4, 2, 6, 3)^t$, should allow to include all possible resonance coupling terms inside a given polyad. In order to see the impact of removing ν_1 and its overtones, as in Section 5.1, an *ab initio* model was built using the scheme $(0, 2, 6, 3)^t$ and the results have been compared to the “full” model. For a proper comparison, $\nu_1 + \nu_2$ and $3\nu_2$ were also removed from the model. Not surprisingly, many line positions of the “light” model were slightly shifted for the $P_n - P_m$ ($n \neq m$) transitions with respect to the “full” model while both the line positions and line intensities of $P_n - P_n$ were similar in the range considered in this work. This can be explained by quite weak resonance couplings between $\nu_1 + \nu_2/3\nu_2$ and $\nu_3/2\nu_4$, making the “ ν_2 ” polyad scheme relevant for the present study. For example, in the “full” model the rovibrational state $|J = 19, C = A_2, \alpha = 11\rangle$ involved in the first transition in Tab. 1 decomposes as $\sim 91.5\%$ of $|\nu_3\rangle$, $\sim 8.5\%$ of $|2\nu_4\rangle$ and less than 0.01% of $|\nu_1 + \nu_2\rangle$ and $|3\nu_2\rangle$.

6 CF₄ database update

The Dijon CF₄ database, also called TFMeCaSDa for TetraFluoroMethane Calculated Spectroscopy Database, and previously built using three different polyad schemes³⁶, has been reviewed and updated. The third scheme, initially used to describe these pure rotational lines of $\nu_3 = 1$, and based on earlier work by Boudon *et al.*¹⁴, has been removed. Instead, we have defined $P_6 - P_6$ in scheme 1, adding 284,350 new transitions in the 1 to 114 cm^{-1} range. This update is already available at <https://vamdc.icb.cnrs.fr/PHP/CF4.php> and will be the subject of a forthcoming publication detailing the latest major update to the Dijon CaSDa24 databases. Table 3 summarizes the changes in the database using this global approach. The total number of calculated lines has increased slightly, but their accuracy is better, as explained in Section 5.

Table 3 Rovibrational transitions in TFMeCaSDa. The polyad scheme is described by the $(c_1, c_2, c_3, c_4)^t$ polyad vector as explained in section 5.

| Transitions | Nb. dipolar | Dipolar wavenumber cm^{-1} | Dipolar intensity $\text{cm}^{-1} / (\text{molecule.cm}^{-2})$ |
|----------------------------------|-------------|--|---|
| Scheme 1 $(0, 2, 6, 3)^t$ | | | |
| $P_6 - P_0$ | 39,086 | 1230 – 1305 | $8 \times 10^{-25} - 8 \times 10^{-22}$ |
| $P_3 - P_0$ | 15,149 | 583 – 682 | $8 \times 10^{-27} - 8 \times 10^{-24}$ |
| $P_8 - P_2$ | 33,430 | 1231 – 1330 | $8 \times 10^{-25} - 1 \times 10^{-20}$ |
| $P_6 - P_6$ | 284,350 | 1 – 114 | $1 \times 10^{-30} - 8 \times 10^{-27}$ |
| Scheme 2 $(3, 0, 4, 2)^t$ | | | |
| $P_6 - P_0$ | 3408 | 1270 – 1283 | $8 \times 10^{-25} - 1 \times 10^{-21}$ |
| Total | 375,423 | | |

7 Conclusion

Using THz CRDS, more than 50 pure rotational transitions $P_6 - P_6 : \nu_3 - \nu_3$ of CF₄ have been measured both in frequency and intensity with unequalled precision. The experimental data have been included in a global fit of the ν_2 polyad series allowing to “clean” the previous line list and to slightly improve the overall RMS in the THz region. Moreover, it was possible for the first time to fit a CF₄ dipole moment parameter using absolute absorption coefficient measurements of individual tetrahedral splitting components, namely the $\tilde{\mu}_{3,3}$ parameter fitted to 106.38(53) mD. For the modelling of the whole rotational spectrum, a set of *ab initio* effective dipole moment parameters was also derived for the first time. The value of the *ab initio* effective parameter $\tilde{\mu}_{3,3}^{ab \textit{ initio}}$ of 117.8 mD is in good agreement with the fitted value. The *ab initio* line list shows that CF₄ rotational transitions belonging to other vibrational states will be accessible in other spectral ranges with the actual degree of sensitivity of the CRDS-THz setup. For example, the $\nu_3 - 2\nu_4$ vibrational state transitions will be accessible at THz frequencies using an AMC covering higher frequencies with a pair of photonic mirrors of suitable dimensions. Nevertheless, the transitions belonging to other fundamental states such as GS–GS or $\nu_4 - \nu_4$ are too weak to be measured with this setup, a sensitivity improvement of several orders is required for their observation. The improvement of cavity stability by its thermal management will allow a higher degree of accumulation to be undertaken.

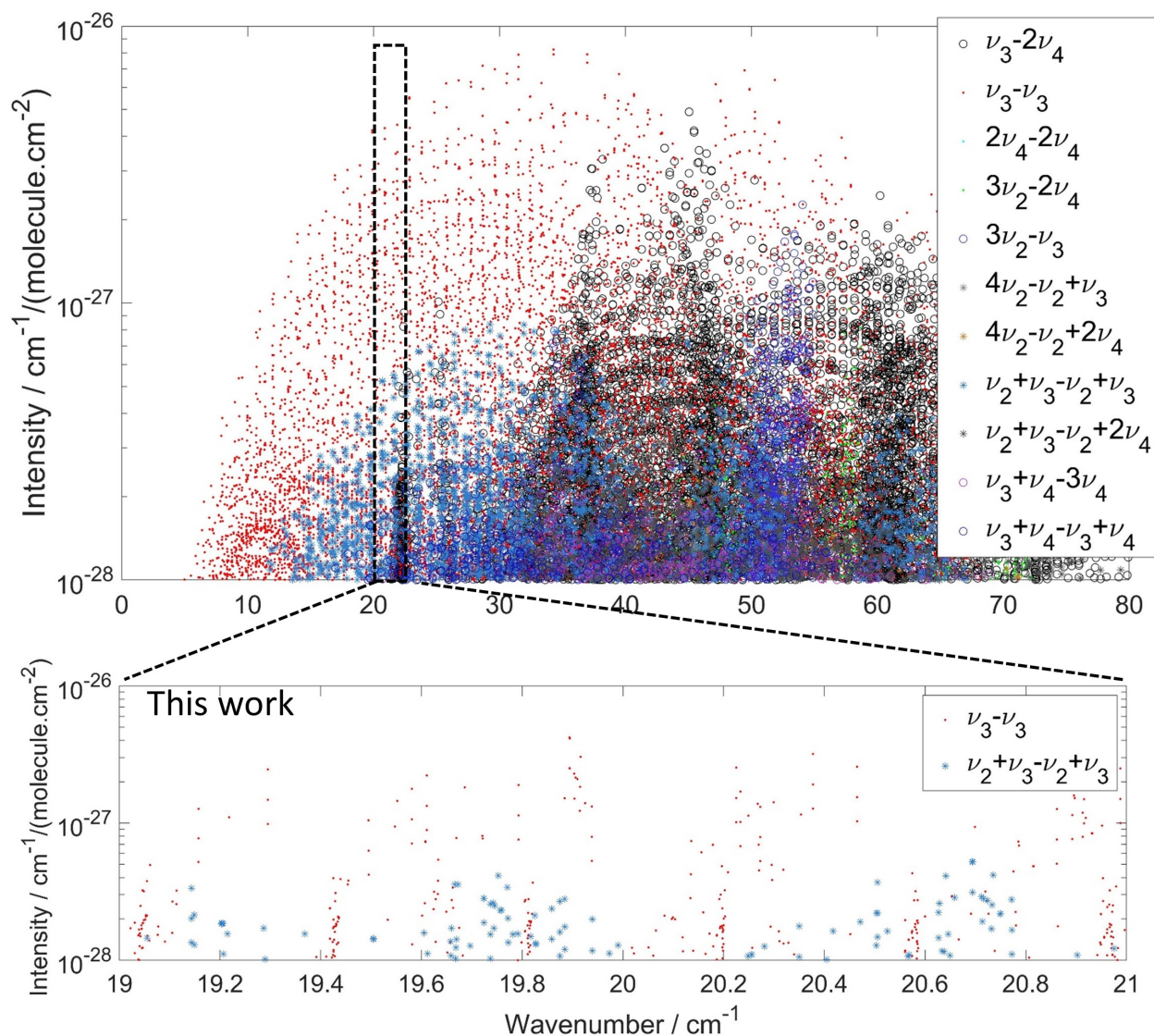


Fig. 10 (Upper panel) Strongest line intensities of the rotational transitions for CF₄ using the *ab initio* effective “global” model described in Section 5.3. (Bottom panel) Detailed portion of the *ab initio* line intensities in the observed range of the present work.

Acknowledgments

The authors thank Marc Fourmentin (LPCA) for writing the procedure to automatically extract the cavity ring down time from the averaged time domain data of each frequency point. The authors would like to acknowledge the financial support of the French Agence Nationale de la Recherche via the projects ANR TIGER (ANR-21-CE30-0048), and ANR METIS (ANR-20-ASTR-0016), the Région Hauts-de-France, the Ministère de l'Enseignement Supérieur et de la Recherche and the European Fund for Regional Economic Development for via the CPER ECRIN program, the Région Hauts-de-France via the Stimule project Deus Marooner. AC is part of the ATMOS project no872081 funded by the H2020-MSCA-RISE-2019 program.

Notes and references

- 1 V. Boudon, J.-P. Champion, T. Gabard, G. Pierre, M. Loëte and C. Wenger, *Environmental Chemistry Letters*, 2003, **1**, 86 – 91.
- 2 C. M. Trudinger, P. J. Fraser, D. M. Etheridge, W. T. Sturges, M. K. Vollmer, M. Rigby, P. Martinerie, J. Mühle, D. R. Worton, P. B. Krummel, L. Paul Steele, B. R. Miller, J. Laube, F. S. Mani, P. J. Rayner, C. M. Harth, E. Witrant, T. Blunier, J. Schwander, S. O'Doherty and M. Battle, *Atmospheric Chemistry and Physics*, 2016, **16**, 11733 – 11754.
- 3 H. De Longueville, L. Clarisse, S. Whitburn, C. Clerbaux, G. Lecomte and P. Coheur, *Journal of Quantitative Spectroscopy and Radiative Transfer*, 2023, **311**, 108755.
- 4 M. Carlos, O. Gruson, C. Richard, V. Boudon, M. Rotger, X. Thomas, C. Maul, C. Sydow, A. Domanskaya, R. Georges,

- P. Soullard, O. Pirali, M. Goubet, P. Asselin and T. Huet, *Journal of Quantitative Spectroscopy and Radiative Transfer*, 2017, **201**, 75–93.
- 5 V. Boudon, M. Carlos, C. Richard and O. Pirali, *Journal of Molecular Spectroscopy*, 2018, **348**, 43–46.
 - 6 A. Cuisset, F. Hindle, G. Mouret, R. Bocquet, J. Bruckhuisen, J. Decker, A. Pienkina, C. Bray, E. Fertein and V. Boudon, *Applied Sciences*, 2021, **11**, 1229.
 - 7 F. Hindle, R. Bocquet, A. Pienkina, A. Cuisset and G. Mouret, *Optica*, 2019, **6**, 1449.
 - 8 C. Elmaleh, F. Simon, J. Decker, J. Dumont, F. Cazier, M. Fourmentin, R. Bocquet, A. Cuisset, G. Mouret and F. Hindle, *Talanta*, 2023, **253**, 124097.
 - 9 M. Rey, I. S. Chizhmakova, A. V. Nikitin and V. G. Tyuterev, *Phys. Chem. Chem. Phys.*, 2018, **20**, 21008–21033.
 - 10 M. Rey, I. S. Chizhmakova, A. V. Nikitin and V. G. Tyuterev, *Phys. Chem. Chem. Phys.*, 2021, **23**, 12115–12126.
 - 11 G. Mouret, M. Guinet, A. Cuisset, L. Croize, S. Eliet, R. Bocquet and F. Hindle, *IEEE Sensors Journal*, 2013, **13**, 133–138.
 - 12 J. van Helden, R. Peverall and G. Ritchie, *Cavity Ring-Down Spectroscopy: Techniques and Applications*, Wiley, 2010, pp. 27–56.
 - 13 D. A. Landman, R. Roussel-Dupre and G. Tanigawa, *The Astrophysical Journal*, 1982, **261**, 732.
 - 14 V. Boudon, M. Carlos, C. Richard and O. Pirali, *Journal of Molecular Spectroscopy*, 2018, **348**, 43–46.
 - 15 C. Bray, A. Cuisset, F. Hindle, G. Mouret, R. Bocquet and V. Boudon, *Journal of Quantitative Spectroscopy and Radiative Transfer*, 2017, **203**, 349–354.
 - 16 M. R. Aliev and J. K. G. Watson, *Higher-order effects in the vibration-rotation spectra of semirigid molecules*, Academic Press, London, 1985.
 - 17 D. Papousek and M. R. Aliev, *Molecular vibrational-rotational spectra*, Elsevier Scientific Publishing Company, Amsterdam-Oxford-New York, 1982.
 - 18 V. Boudon, J.-P. Champion, T. Gabard, M. Loëte, M. Rotger and C. Wenger, *Handbook of High-Resolution Spectroscopy*, Wiley, Chichester, West Sussex, United Kingdom, 2011, vol. 3, pp. 1437–1460.
 - 19 M. Rey, *The Journal of Chemical Physics*, 2022, **156**, 224103.
 - 20 C. Wenger, V. Boudon, M. Rotger, J. P. Sanzharov and J. P. Champion, *Journal of Molecular Spectroscopy*, 2008, **251**, 102–113.
 - 21 M. Takami, *J. Chem. Phys.*, 1980, **73**, 2665–2672.
 - 22 M. Takami, *J. Chem. Phys.*, 1981, **74**, 4276–4285.
 - 23 H. Berger, *J. Phys.*, 1977, **38**, 1371–1375.
 - 24 J. V. Auwera, 2023, Private Communication.
 - 25 I. E. Gordon, L. S. Rothman, R. V. C. Hill and, Y. Tan, P. F. Bernath, M. Birk, V. Boudon, A. Campargue, K. V. Chance, B. J. Drouin, J.-M. Flaud, R. R. Gamache, J. T. Hodges, D. Jacquemart, V. I. Perevalov, A. Perrin, K. P. Shine, M.-A. H. Smith, J. Tennyson, G. C. Toon, H. Tran, V. G. Tyuterev, A. Barbe, A. Csaszar, M. V. Devi, T. Furtenbacher, J. J. Harrison, A. Jolly, T. Johnson, T. Karman, I. Kleiner, A. A. Kyuberis, J. Loos, O. M. Lyulin, S. T. Massie, S. N. Mikhailenko, N. Moazzen-Ahmadi, H. S. P. Müller, O. V. Naumenko, A. V. Nikitin, O. L. Polyansky, M. Rey, M. Rotger, S. Sharpe, K. Sung, E. Starikova, S. A. Tashkun, J. V. Auwera, G. Wagner, J. Wilzewski, P. Wcisło, S. Yu and E. J. Zak, *J. Quant. Spectrosc. Radiat. Transfer*, 2017, **203**, 3–69.
 - 26 M. Rey, A. V. Nikitin and V. G. Tyuterev, *ApJ*, 2017, **847**, 1.
 - 27 M. Rey, A. V. Nikitin, Y. L. Babikov and V. G. Tyuterev, *J Mol. Spectrosc.*, 2016, **327**, 138–158.
 - 28 A. Domanskaya, K. Berezkin, G. Li, H. Bohlius, M. Kim, J. Harrison and V. Ebert, *J. Quant. Spectrosc. Radiat. Transf.*, 2023, **311**, 108790.
 - 29 J. K. G. Watson, *Mol. Phys.*, 1968, **15**, 479–490.
 - 30 V. Tyuterev, S. Tashkun, M. Rey and A. Nikitin, *Molecular Physics*, 2022, **120**, e2096140.
 - 31 J. Van Vleck, *Phys. Rev.*, 1929, **33**, 467.
 - 32 J. P. Champion, M. Loëte and G. Pierre, *Spherical Top Spectra*, Academic Press, K N Rao A Weber, San Diego, 1992.
 - 33 A. V. Nikitin, J. P. Champion and V. G. Tyuterev, *J. Mol. Spectrosc.*, 1997, **182**, 72–84.
 - 34 V. Boudon, O. Pirali, P. Roy, J.-B. Brubach, L. Manceron and J. Vander Auwera, *Journal of Quantitative Spectroscopy and Radiative Transfer*, 2010, **111**, 1117–1129.
 - 35 M. Rey, A. V. Nikitin and V. G. Tyuterev, *Phys. Chem. Chem. Phys.*, 2013, **15**, 10049–10061.
 - 36 C. Richard, V. Boudon and M. Rotger, *Journal of Quantitative Spectroscopy and Radiative Transfer*, 2020, **251**, 107096.